RSC Advances

PAPER

View Article Online
View Journal | View Issue

Check for updates

Cite this: *RSC Adv.*, 2023, **13**, 36209

Calcined chicken eggshell-derived biomimetic nano-hydroxyapatite as a local drug-delivery aid for doxycycline hyclate: characterization, bioactivity, cytotoxicity, antibacterial activity and *in vitro* release study

Mashrafi Bin Mobarak,[a] M. Nahidul Islam,[b] Fariha Chowdhury,[c] Md. Najem Uddin,[d] Md. Sahadat Hossain,[a] Monika Mahmud,[a] Umme Sarmeen Akhtar,[a] Nazmul Islam Tanvir,[d] A. F. M. Mustafizur Rahman[b] and Samina Ahmed *[ad]

The integration of bioactive substances with antibiotics has been extensively pursued for the treatment of osteomyelitis. These materials, also known as biomaterials, can serve both as bone replacements and targeted drug delivery systems for antibiotics. In this study, biomimetic nano-hydroxyapatite (nHAp) was synthesized *via* the coprecipitation technique where waste chicken eggshell (WCE) was employed as the source of Ca. Heat treatment was performed at four different temperatures (100 °C, 300 °C, 600 °C and 900 °C). Subsequently, the samples were characterized using XRD, FTIR spectroscopy, Raman spectroscopy, FESEM, EDX, XPS, DLS hydrodynamic size and zeta potential analysis. Also, their biomedical effectiveness was evaluated in terms of cytotoxicity, hemolysis, antibacterial performance, and bioactivity. Doxycycline hyclate (DOXh) was loaded in the synthesized nHAp samples, and subsequently its *in vitro* release was studied under stirring in simulated body fluid (SBF). The DOXh release kinetics was evaluated, and it was found that the first-order model was the best fitted kinetic model describing the release of DOXh from the nHAp samples, except for nHAp100, which was best described by the Korsmeyer–Peppas model. The nHAp synthesized utilizing WCE showed excellent potential for biomedical application and can be used as a drug delivery agent for antibiotics, such as DOXh.

Received 15th October 2023
Accepted 21st November 2023

DOI: 10.1039/d3ra07010g

rsc.li/rsc-advances

Open Access Article. Published on 12 December 2023. Downloaded on 2/8/2026 7:38:46 PM.
This article is licensed under a Creative Commons Attribution-NonCommercial 3.0 Unported Licence.

1. Introduction

Bone defects, which are caused by various reasons, such as bone diseases, infections, and accidents, are also associated with further trauma given that their treatment is very costly with long treatment times and the torment from unsuccessful treatment results.[1] Among the causes of bone defects, bone infection is greatly associated with various microorganisms, which, when raised to the level of inflammation (acute or chronic), causes osteomyelitis.[2] The infectious microorganisms show hostility in various places of the bone, such as the marrow, cortex, and adjacent tissues that are known to be soft in nature. People of any age are susceptible to this disease, which can affect any type of bone. This results in a traumatic experience, and patients with diabetes face the worst-case scenarios. Among the microorganisms responsible for osteomyelitis, *Staphylococcus aureus*, Gram-positive bacteria, has been found to be the most common (approximately 75% of all cases), with its virulence affecting various extracellular and cell-associated factors.[3–5] In this case, to fight osteomyelitis, a combination of operative debridement, bone defect filling, and antibiotic therapy is usually used.[6,7] Generally, antibiotic therapy is comprised of intravenous and oral administration for a period of approximately 3 weeks each, but nowadays it is for longer periods in most cases.[8–10] To ensure the necessary dosage of antibiotics at the infected sites, a high dosage is usually recommended given that the drugs have a very low efficiency of penetration from the blood stream to the targeted site.[11,12]

The prolonged administration of antibiotics at high dosages results in systemic toxicity together with detrimental effects on organs, such as the liver and kidney, in addition to the upsurge in antibiotic and multidrug resistance.[13] One of the crucial reasons for antibiotic resistance is the formation of a biofilm,

[a]*Institute of Glass and Ceramic Research and Testing (IGCRT), Bangladesh Council of Scientific and Industrial Research (BCSIR), Dhaka-1205, Bangladesh. E-mail: shanta_samina@yahoo.com*

[b]*Department of Applied Chemistry and Chemical Engineering, University of Dhaka, Dhaka-1000, Bangladesh*

[c]*Biomedical and Toxicological Research Institute (BTRI), Bangladesh Council of Scientific and Industrial Research (BCSIR), Dhaka-1205, Bangladesh*

[d]*BCSIR Laboratories Dhaka, Bangladesh Council of Scientific and Industrial Research (BCSIR), Dhaka-1205, Bangladesh*

© 2023 The Author(s). Published by the Royal Society of Chemistry

Open Access Article. Published on 12 December 2023. Downloaded on 2/8/2026 7:38:46 PM. This article is licensed under a Creative Commons Attribution-NonCommercial 3.0 Unported Licence.

which protects bacteria from antibiotics, and even makes them a thousand times more resistant than bacteria without a biofilm.[14] Due to these reasons, patients must take an excessive amount of antibiotics to fight against bacteria, and thus researchers have devoted their efforts to looking for better alternatives.[15]

To date, although there have been significant revolutions in the fields of surgery and antibiotic treatment, the localized delivery of antibiotics is an approach widely accepted by researchers given that it offers solutions to problems such as systemic toxicity and excessive administration given that it increases the therapeutic concentration of the drug at the targeted site.[2,8,11,15] Drug delivery systems for the localized delivery of drugs are designed with two types of carriers, *i.e.*, biodegradable and non-biodegradable. Although non-biodegradable delivery systems have shown promising results, they are limited by the fact that the carrier needs to be changed or withdrawn, which is not the case for biodegradable local drug carriers.[8,16] Biomaterials are the most preferred carriers when designing a biodegradable local drug delivery system and an amalgamation of biomaterial-antibiotic helps in treating osteomyelitis to a great extent.[2,17]

Hydroxyapatite ($Ca_{10}(PO_4)_6(OH)_2$) has been recognized as a gold standard biomaterial due to its similarity in structure and behavior to human bone.[18–25] In addition, hydroxyapatite (HAp) possesses superb biocompatibility, osteoconductivity, bioactivity, non-toxicity, non-inflammatory properties, and excellent stability.[26] HAp has already been investigated for the localized delivery of drugs such as ciprofloxacin,[27] amoxicillin,[15] vancomycin,[29] and gentamicin.[28,30] The loading of drugs is carried out either *via* a facile adsorption process or solid-state mixing, where the latter is responsible for uncontrolled release of the drug. In this case, the existence of positively charged calcium and negatively charged phosphorus sites in HAp facilitates the adsorption process.[2,31] Also, the synthesis of nano-sized HAp carriers makes the drug delivery system even more desirable due to the resulting superior loading and adsorption and more controlled delivery.

In our study, we synthesized nHAp using the coprecipitation method, employing chicken eggshells, a byproduct of poultry, as the source of calcium. To date, many studies have reported the superior workability of eggshell-derived nHAp compared to synthetic nHAp. The absence of certain minerals that constitute tooth apatite, inferior sinterability in terms of hardness and density, lower bioactivity, expensive raw materials, *etc.* are some of the shortcomings of synthetic nHAp, shifting the focus to the waste-derived synthesis of nHAp.[32–34] nHAp was evaluated as a localized drug delivery carrier for DOXh, a potent broad-spectrum antibiotic effective against both Gram-positive and Gram-negative bacteria.[35] DOXh is water-soluble and falls in the family of tetracyclines. Besides its widespread use in the treatment of skin infections such as chlamydia, cholera, and syphilis, DOXh has also found application in fighting osteomyelitis.[5,36,37] Numerous studies have investigated the DOXh loading-release profile of synthetic HAp[38] as well as scaffolds prepared by combining HAp with synthetic/natural polymer blends such as poly(lactide-*co*-glycolide),[39] polycaprolactone/gelatin,[40] alginate,[41] collagen,[42] and polylactic acid.[43] However, none of these studies focused on the synthesis of bio-waste-derived HAp and the effect of calcination temperature on the loading and release of DOXh. The objective of this study was to analyse the adsorption of DOXh molecules on the surface of nHAp calcined at different temperatures, assess the drug release, investigate its impact on epithelial cells (cytotoxicity) and red blood cells (hemolysis), *in vitro* formation of an apatite layer and estimate its antibacterial properties. An alternative hypothesis is that the calcination temperature of nHAp has effect on the DOXh loading and release given that calcination results in changes in certain properties of HAp.[44] Furthermore, the potential of bio-waste-derived nHAp to act as a local carrier of DOXh was evaluated, contributing to the scientific research in this field.

2. Materials and methods

2.1 Materials

WCE was collected from nearby cafeterias of the Dhaka University campus (23°43′32.0″N 90°24′13.2″E). *ortho*-Phosphoric acid (H_3PO_4) (Merck, Germany) was the P source and ammonia solution (NH_4OH) was used for pH adjustment. The reagents used for the preparation of SBF solution are tabulated in Table 1. Doxycycline hyclate BP was generously donated by ACI Pharmaceuticals, Bangladesh. No further purification of these chemicals was done, and DI (de-ionized) water was used to prepare all solutions and experimentation.

2.2 Methods

2.2.1 Preparation of eggshell powder. The preparation of eggshell powder was reported in our previous work.[45] Briefly, the collected WCEs were washed thoroughly, boiled for 2 h, their membranes removed and oven dried. Subsequently, the dried eggshell fragments were ball milled at 450 rpm for 2 h, which produced fine eggshell powder.

2.2.2 Synthesis of nHAp. The eggshell powder was subjected to calcination at 900 °C for a duration of 1 h at a heating rate of 5 °C min^{-1} to transform the $CaCO_3$ in the eggshells into CaO.[46] This process eliminated volatile impurities and organic membranes, resulting in the production of pure CaO. A quantity of 5.6 g of CaO was dissolved in DI water to create a 100 mL solution. This solution was stirred for 1 h, yielding a warm $Ca(OH)_2$ solution. The exothermic reaction confirmed the formation of $Ca(OH)_2$. A 0.6 M 100 mL solution of H_3PO_4 was prepared by dissolving 4.04 mL of H_3PO_4 in DI water. The gradual addition of H_3PO_4 to the $Ca(OH)_2$ solution, while maintaining a Ca/P ratio of 1.67 led to the formation of a white precipitate of nHAp. The solution pH was controlled at around 11 by adding NH_4OH, and stirring was continued for an additional hour. Afterward, the solution was allowed to age for 24 h, filtered, and subsequently dried in an oven. The resulting dried nHAp powder was divided into four parts and individually subjected to calcination at temperatures of 100 °C, 300 °C, 600 °C, and 900 °C, each for 30 min, at a heating rate of 5 °C min^{-1}. The four nHAp samples were denoted as nHAp100, nHAp300,

 © 2023 The Author(s). Published by the Royal Society of Chemistry

Open Access Article. Published on 12 December 2023. Downloaded on 2/8/2026 7:38:46 PM.
This article is licensed under a Creative Commons Attribution-NonCommercial 3.0 Unported Licence.

Table 1 Name, quality and quantity of reagents used for the preparation of SBF

Order	Reagent	Procurement	Purity (%)	M.W (g mol^{-1})	Amount as per[47] (g)	Amount in this study (g)
1	NaCl	Merck	99.5	58.44	6.547	6.545
2	$NaHCO_3$	Merck	99.5	84.01	2.268	2.268
3	KCl	Merck	99.5	74.55	0.373	0.373
4	Na_2HPO_4	Merck	98	156.01	0.178	0.176
5	$MgCl_2 \cdot 6H_2O$	Merck	99	203.30	0.305	0.305
6	$CaCl_2 \cdot 2H_2O$	Merck	99.5	147.02	0.368	0.368
7	Na_2SO_4	Merck	99	142.04	0.071	0.072
8	$(CH_2OH)_3CNH_2$	Scharlau	99.8	121.14	6.057	6.057

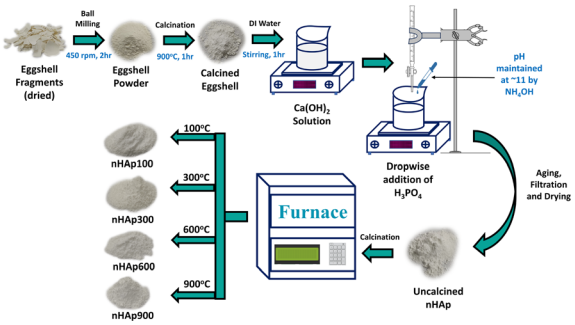

Fig. 1 Synthesis scheme of nHAp by wet chemical process utilizing chicken eggshell.

nHAp600, and nHAp900, respectively. The aforementioned synthesis scheme is illustrated in Fig. 1.

2.2.3 Preparation of SBF solution. Simulated body fluid (SBF), also known as metastable buffer solution, was prepared according to the work of Tas,[47] which is a modified preparation method compared to the previously reported work of Kokubo *et al.*[48] The modification was in terms of increasing the concentration of HCO_3 from 4.2 mM to 27 mM, which eliminated the bicarbonate ion deficiency associated with traditional methods. Also, the Cl^- ion concentration was reduced from 147.8 mM to 125 mM given that human blood plasma contains only 103 mM of Cl^- ions.[49] Table 1 presents a summary of the preparation of the SBF solution (pH 7.4).

2.2.4 Characterization. The samples' phase confirmation was conducted using X-ray powder diffraction (Rigaku Smart Lab; 2θ range: 5°–70°; scan rate: 35° min^{-1}; X-ray generation: 40 kV, 50 mA; CuKα radiation of wavelength λ = 1.54060 Å). The phase identification was accomplished by comparing the data with the ICDD database. Crystallographic parameters such as lattice parameters, unit cell volume, crystallite size, dislocation density, degree of crystallinity and micro-strain were calculated using eqn (1)–(6), respectively, as follows:[23,50]

$$\frac{1}{d^2} = \frac{4}{3}\left(\frac{h^2 + hk + k^2}{a^2}\right) + \frac{l^2}{c^2} \quad (1)$$

$$V = \frac{\sqrt{3}}{2}a^2c \quad (2)$$

$$D = \frac{k\lambda}{\beta_{(211)}\cos\theta} \quad (3)$$

$$\delta = \frac{1}{D^2} \quad (4)$$

$$X_c = \left(\frac{K_a}{\beta_{(002)}}\right)^3 \quad (5)$$

$$\varepsilon = \frac{\beta_{(211)}}{4\tan\theta} \quad (6)$$

where d = d-spacing, which is also known as the interplanar distance; h, k and l = Miller indices; a, b and c = unit cell parameters representing length in three dimensions; D = crystallite size; K = constant representing the shape factor, which is considered to be 0.9 for most materials; λ = wavelength of X-rays generated through Cu tube (CuKα radiation of 0.15406 nm); $\beta_{(211)}$ = full width half maximum (FWHM) at (211) crystal plane; θ = diffraction angle; δ = dislocation density; X_C = degree of crystallinity; K_a = constant (0.24 for most HAp) and ε = micro-strain.

FTIR (IR Prestige-21, Shimadzu Corp. mounted with ATR) and Raman (HORIBA Macro-RAM™ with 785 nm wavelength laser) spectroscopic analysis was done to detect the functional groups present on the nHAp samples. The morphology and elemental analysis of the prepared samples were carried out by FESEM and EDX analysis, respectively (JEOL JSM-7610F). The DLS hydrodynamic size and surface charge of the synthesized samples were evaluated using a Malvern Zetasizer Ultra. The assessment of surface chemistry was conducted using an XPS instrument (Thermo Scientific K-Alpha).

2.2.5 Cytotoxicity study. The cytocompatibility of the synthesized nHAp samples was evaluated based on the cell viability of the Vero cell line, which is the extracted kidney epithelial cells of the African green monkey. The Vero cells (procured from ThermoFisher Scientific, UK) were maintained in Dulbecco's modified Eagle medium (DMEM), which was comprised of 1% penicillin-streptomycin (mixed in a 1 : 1 ratio), 0.2% gentamycin, and 10% FBS (fetal bovine serum). The Vero cells (1.5×10^4/100 μL) were seeded on a 96-well plate, and incubation was carried out for 24 h under 5% carbon dioxide at 37 °C. After incubation, 25 μL of the sample was added to each well, and the cytocompatibility assessment was done for 48 h

Open Access Article. Published on 12 December 2023. Downloaded on 2/8/2026 7:38:46 PM.
This article is licensed under a Creative Commons Attribution-NonCommercial 3.0 Unported Licence.

under a trinocular microscope (Optika, Italy), and the number of cells was counted by an automated cell counter (hemocytometer). Duplicate wells were used for each sample, and a similar procedure was done for all the nHAp samples. The cell viability was calculated as follows:[21]

$$\text{Cell viability} = \frac{\text{number of live cells}}{\text{Total number of cells}} \times 100\% \quad (7)$$

2.2.6 Bioactivity study. The assessment of the bioactivity of the prepared nHAp samples involved the immersion of 100 mg of the sample in a 100 mL SBF solution, keeping it in a Duran bottle with lid, and placing it in an incubator for 3 weeks at 37 °C. After 3 weeks, the samples were separated by decantation and oven dried. The dried samples were then analyzed by FESEM to confirm the formation of apatite on the nHAp surface.

2.2.7 Antibacterial activity study. The assessment of the antibacterial effectiveness of the synthesized nHAp carriers (nHAp100, nHAp300, nHAp600, and nHAp900) was carried out using the agar-well diffusion technique[51] against *Escherichia coli* (Gram −ve, ATCC 11303) and *Staphylococcus aureus* (Gram +ve, ATCC 9144). The bacterial colonies were grown in Mueller-Hinton broth (at 120 rpm and 37 ± 2 °C). Sterile micropipette tips were used to create wells with a 6 mm diameter on the agar plates. The nHAp carriers (400 μg mL^{-1}) together with 5% dimethyl sulfoxide (DMSO) were loaded on the wells, which acted as a negative control. To serve as a positive control, a kanamycin disk with a 30 μg dosage was employed. The agar plates were kept at 4 °C for 3 h to counteract the penetration and diffusion of nHAp particles. Subsequently, the agar plates were placed in an incubator for a 24 h period, and the diameter of the inhibition zone was recorded.

2.2.8 Hemolytic study. Human blood samples were obtained using heparin as an anticoagulant, and then subjected to incubation at 37 °C for 1 h. The nHAp carriers were made into solutions of 400 μg mL^{-1} concentration using phosphate buffer saline (PBS). Then, each of the four samples was mixed with 0.4 mL of the incubated blood samples, and further incubated for 1 h. A similar procedure was followed, but without the addition of any nHAp carrier. In this case, PBS served as the negative control and deionized water served as the positive control. Following incubation, the samples underwent centrifugation at 5000 rpm for 5 min. Subsequently, the supernatant was collected, and its absorbance was quantified at 545 nm employing a UV-Vis spectrophotometer. The absorbance data reflects the release of hemoglobin as a result of red blood cell lysis, which could be used to assess the hemocompatibility of the nHAp carriers.[52] The percentage of hemolysis in the blood sample can be computed using the following formula:[53]

$$\%\ \text{Hemolysis} = \frac{D_t - D_{nc}}{D_{pc} - D_{nc}} \times 100 \quad (8)$$

where D_t = absorbance of the nHAp solution, D_{nc} = absorbance of the negative control and D_{pc} = absorbance of the positive control.

2.2.9 DOXh loading study. Initially, 50 ppm stock solution of DOXh was prepared, from which 50 mL drug solution was taken and 100 mg of nHAp carrier was suspended. The slurries were subjected to sonication for 10 min to ensure the proper dispersion and reduce the agglomeration of the nHAp particles. After sonication, the solutions were stirred in a magnetic stirrer for 2 h at 25 ± 1 °C. The nHAp samples were separated from the drug solution by vacuum filtration with a micro filter (Ultipor® 0.2 μm). The residues were washed a few times with DI and acetone to remove excess drug from the surface. The absorbance of the stock solution and the filtrates was measured using a UV-Vis spectrophotometer (Hitachi U-2910) at 273 nm to calculate the DOXh loading capacity (eqn (9)) and entrapment efficacy (eqn (10)).[54] A calibration curve was plotted to determine the unknown concentration of the drug.

$$\text{Loading capacity } (\%) = \frac{\text{total drug encapsulated}}{\text{Weight of carrier}} \times 100 \quad (9)$$

$$\text{Entrapment efficacy } (\%) = \frac{\text{initial con. of drug} - \text{conc. of drug in filtrate}}{\text{initial conc. of drug}} \times 100 \quad (10)$$

2.2.10 *In vitro* release study. The release of DOXh was observed by suspending 50 mg of DOXh-loaded nHAp carrier in 50 mL SBF solution (pH 7.4) at 37 °C under constant stirring. The amount of DOXh released was measured by taking aliquots from the SBF release medium at different intervals and subjecting them to spectrophotometric measurement at 273 nm. The amount of solution taken from the release media was replenished by fresh SBF solution. The cumulative DOXh release% was calculated using the following equation:

$$\text{Cumulative DOXh release } (\%) = \frac{\text{amount of DOXh in release media}}{\text{Initial amount of DOXh loaded on HAp}} \times 100 \quad (11)$$

2.2.11 Ethical statement

All tests were conducted following the guidelines of "IGCRT." The experiments received approval from the Ethics Committee at "BCSIR," and informed consent was obtained from all human participants involved in the study (Ref: 1GCRT/R&D research/2022-2024/01; Date: 04.10.2022).

3. Results and discussion

3.1 X-ray diffraction analysis

X-Ray powder diffractometry was employed to identify the phase and its purity and quantify the crystallographic parameters that play a vital role in the properties of hydroxyapatite.[25] Fig. 2 presents the XRD patterns of the synthesized nHAp samples, depicting the formation of nHAp at different temperatures with undisrupted stability even at 900 °C. Compared with the ICDD database, JCPDS File No. #01-084-1998 was the closest match with nHAp100 and nHAp300.[55] Alternatively, nHAp600 closely matched with JCPDS File No. #00-009-0432 [56] and nHAp900 had the closed match with JCPDS File No. #01-086-0740.[57] The

© 2023 The Author(s). Published by the Royal Society of Chemistry

Open Access Article. Published on 12 December 2023. Downloaded on 2/8/2026 7:38:46 PM.
This article is licensed under a Creative Commons Attribution-NonCommercial 3.0 Unported Licence.

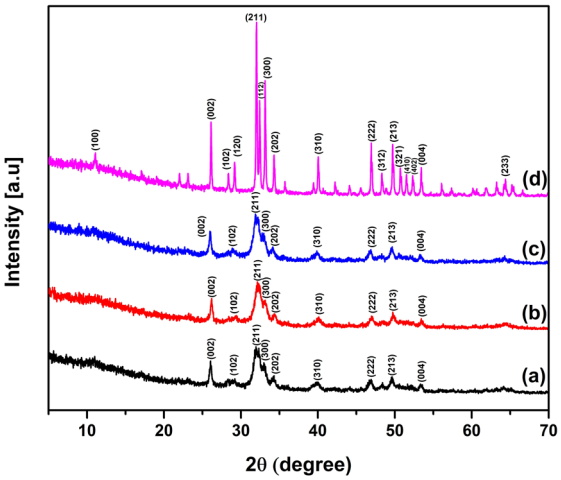

Fig. 2 XRD patterns of prepared nHAp samples: (a) nHAp100, (b) nHAp300, (c) nHAp600 and (d) nHAp900.

diffraction patterns of nHAp100, nHAp300 and nHAp600 showed broad contour in the 2θ diffraction angle range of 30° to 35°. The crystal planes observed in this range include (211), (300) and (202), while the (002), (310), (222), (213) and (004) planes were observed outside the contour. All these planes are characteristic for the HAp phase. In the case of nHAp900, sharper and well-defined peaks were observed. One isolated peak was observed at the diffraction angle of 11°, which corresponds to the (100) crystal plane of HAp. At the elevated temperature of 900 °C, no peaks of β-TCP (tri-calcium phosphate) were observed, confirming the mono-phasic nature of nHAp900. With an increase in temperature, more intense peaks with a lower peak width were observed, which was also reported in the literature.[22,58]

The quantitative analysis based on the XRD patterns (crystallite size, dislocation density, degree of crystallinity, micro-strain and specific surface area) is illustrated in Fig. 3 and the unit cell parameters are tabulated in Table 2.

As the calcination temperature increased, the crystallite size and the degree of crystallinity also increased. In contrast, the dislocation density and micro-strain of the nHAp samples decreased at elevated temperatures.

3.2 FTIR analysis

FTIR is a widely employed technique used to determine the functional groups present in unknown samples. To identify the functional groups in the prepared nHAp samples, their FTIR spectra were recorded, as shown in Fig. 4a. All the spectra show similar patterns except for some slight differences. The patterns are typical for HAP, where the presence of unwanted or unreacted groups was not detected. The characteristic apatite phase was confirmed by the well-defined bands in the range of 559 cm^{-1} to 1091 cm^{-1}.[59,60] The bands around ~470 cm^{-1} correspond to the O–P–O symmetric bending modes (ν_2), while the bands in the range of 557 cm^{-1} to 601 cm^{-1} correspond to the O–P–O asymmetric bending modes (ν_4).[21]

The structural OH^- group of the prepared HAp samples was observed at 632–634 cm^{-1} and ~3572 cm^{-1}.[61] The observed bands at 873 and 1421 cm^{-1} for HAp100 and 877 cm^{-1} and 1415 cm^{-1} for HAp300 are attributed to the CO_3^{2-} group. In contrast, none of these peaks were detected for HAp600 and HAp900. The O–P–O symmetric (ν_1) and asymmetric (ν_3) stretching bands were detected at ~960 cm^{-1} and ~1024 cm^{-1}, respectively. The absence of bands for adsorbed H_2O indicates the appropriate storage and handling of the samples. The FTIR spectra of DOXh and the DOXh-loaded nHAp samples were also recorded (shown in

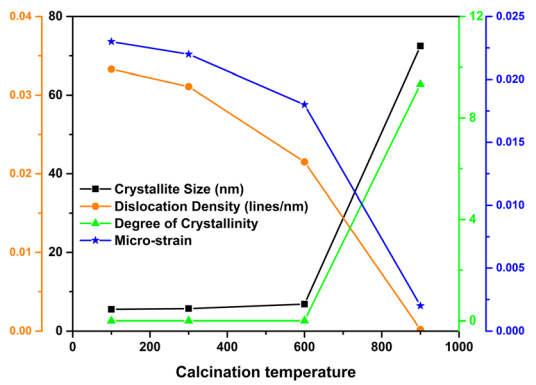

Fig. 3 Relation between crystallite size, dislocation density, degree of crystallinity and micro-strain of nHAp with respect to calcination temperature.

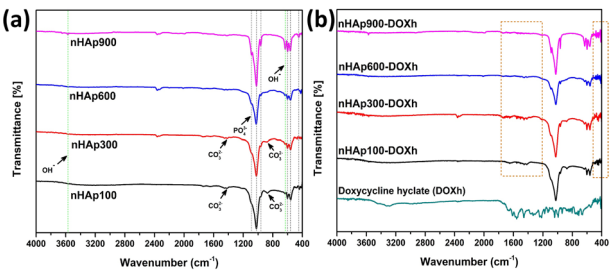

Fig. 4 FTIR spectra of (a) nHAp samples (nHAp100, nHAp300, nHAp600 and nHAp900) and (b) doxycycline hyclate (DOXh) and DOXh-loaded nHAp samples.

Table 2 Lattice parameters of the synthesized HAp samples

Sample name	Lattice parameters (experimental)	Lattice parameters (standard)	JCPDS file no.
nHAp100	$a = b = 9.4099$ Å and $c = 6.8322$ Å, $V = 523.92$ Å^3	$a = b = 9.4166$ Å and $c = 6.8745$ Å, $V = 527.91$ Å^3	#01-084-1998
nHAp300	$a = b = 9.3633$ Å and $c = 6.8298$ Å, $V = 518.56$ Å^3	$a = b = 9.4166$ Å and $c = 6.8745$ Å, $V = 527.91$ Å^3	#01-084-1998
nHAp600	$a = b = 9.4091$ Å and $c = 6.8550$ Å, $V = 525.57$ Å^3	$a = b = 9.4180$ Å and $c = 6.8840$ Å, $V = 528.80$ Å^3	#00-009-0432
nHAp900	$a = b = 9.3815$ Å and $c = 6.8350$ Å, $V = 510.97$ Å^3	$a = b = 9.3520$ Å and $c = 6.8820$ Å, $V = 521.26$ Å^3	#01-086-0740

Open Access Article. Published on 12 December 2023. Downloaded on 2/8/2026 7:38:46 PM.
This article is licensed under a Creative Commons Attribution-NonCommercial 3.0 Unported Licence.

Fig. 4b). The inclusion of DOXh in the nHAp samples was mainly confirmed by the appearance of new peaks at very low intensities in the range of 400–520 cm^{-1} and 1210–1770 cm^{-1}.

3.3 Raman analysis

The Raman spectroscopic analysis of the synthesized nHAp samples was carried out to investigate the Raman shifts of the existing functional groups and confirm the presence of the apatite phase. The Raman spectra of the nHAp samples are presented in Fig. 5. Raman analysis is useful for materials such as HAp to describe their crystallinity with respect to different reaction conditions including pH, reaction time, calcination temperature, and Ca/P ratio.[62]

Consistent with the XRD analysis, it was evident that the calcination temperature significantly influenced the crystallinity of the synthesized nHAp samples. The formation of a crystalline phase at 900 °C was well evident in the Raman spectrum of nHAp900, which has the highest Raman intensity peak among the samples at 965 cm^{-1}. Inversely, nHAp100, nHAp300, and nHAp600 have an amorphous phase with a low, intense peak at around 965 cm^{-1}, which is consistent with the XRD spectra. The peak at ~965 cm^{-1} corresponds to the ν_1 stretching of P–O, which is also defined as the symmetric stretching of the PO_4^{3-} group.[63] The other Raman shifts observed correspond to: (i) ν_2 symmetrical bending (O–P–O) in the range of 429 to 433 cm^{-1}, (ii) ν_3 asymmetric P–O stretching at 1049 to 1079 cm^{-1} (only observed for nHAp900) and (iii) ν_4 anti-symmetrical bending at 555 to 643 cm^{-1} for all the nHAp samples.[64–67]

3.4 FESEM and EDX study

FESEM was used to perform the morphological investigation of the produced nHAp samples. Fig. 6a, d, g, and j present the FESEM images of nHAp100, nHAp300, nHAp600, and nHAp900, respectively. According to the images, the particles of nHAp100 exist in agglomerated form, and their shape includes a long cylindrical rod, which is irregularly structured.

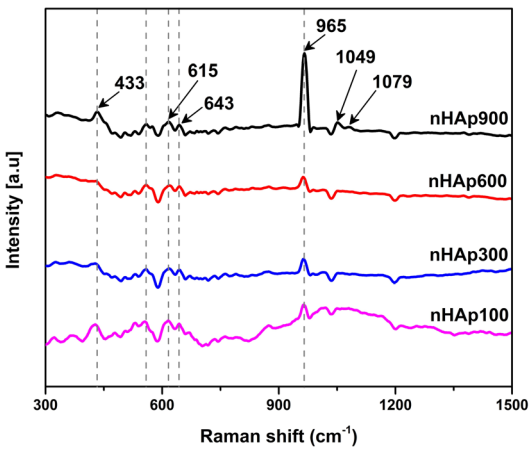

Fig. 5 Raman spectroscopic analysis of prepared nHAp samples calcined at 100 °C, 300 °C, 600 °C and 900 °C.

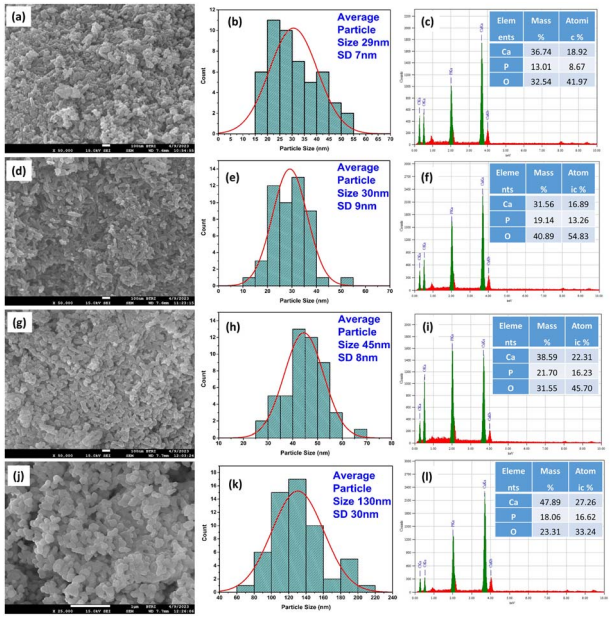

Fig. 6 FESEM, particle size histogram and EDX spectra of nHAp100 (a, b and c), nHAp300 (d, e and f), nHAp600 (g, h and i) and nHAp900 (j, k and l), respectively.

Alternatively, less agglomerated particles were observed for the nHAp300, nHAp600, and nHAp900 samples. As the calcination temperature increased, several phenomena occurred, including sintering and grain growth, elevated thermal energy and particle mobility, elimination of defects and dislocations, Ostwald ripening, and redistribution of atoms. These processes contributed to the reduction in agglomeration and increase in crystallite size. This observation is consistent with the findings reported in previous studies.[68–70] In the case of calcination at 900 °C, smaller and more agglomerated particles sintered together and formed large agglomerates, causing the nHAp900 particles to be the largest among the samples.[71] The particles of nHAp300 and nHAp600 were mostly cylindrical rod-shaped; however, shorter lengths with much wider particles were seen for nHAp600. Interestingly, the cylindrical rod shape was not seen for nHAp900; rather, rouletted, oval, and irregular flat plate shapes were observed. Thus, with an increase in the calcination temperature, the cylindrical rod shapes were transformed into a more rouletted plate shape. The particle size of the samples was measured based on these images, following our previously reported protocol.[72] A minimum of 50 discrete particles with a clearly detectable boundary were considered for each measurement. The nano-structured form of the samples was confirmed by the particle size histograms, as shown in Fig. 6b, e, h, and k. With an increase in the calcination temperature, the particle size of the samples also increased, with nHAp100 having the lowest particle size and nHAp900 having the highest particle size. This is consistent with the crystallite size variation extrapolated from the XRD analysis.

The elemental analysis of the samples was done in terms of EDX, as shown in Fig. 6c, f, i and l. The elements present in the nHAp structure, *i.e.*, Ca (K_a and K_b), P (K_a) and O (K_a) were

© 2023 The Author(s). Published by the Royal Society of Chemistry

Open Access Article. Published on 12 December 2023. Downloaded on 2/8/2026 7:38:46 PM.
This article is licensed under a Creative Commons Attribution-NonCommercial 3.0 Unported Licence.

confirmed together with their quantitative analysis. A peak for C (K_a) was detected, which originated from the carbon tape onto which the samples were placed. The Ca/P ratios of the nHAp samples based on EDX analysis are as follows: nHAp100 (2.18), nHAp300 (1.27), nHAp600 (1.37), and nHAp900 (1.64). The Ca/P ratio of nHAp900 is the closest to the theoretical Ca/P ratio of nHAp (1.67). This ratio was the highest for nHAp100, which then decreased with the calcination temperature, and eventually increased to 1.64 at 900 °C calcination. According to the work of Agbabiaka *et al.*, the Ca/P ratio of waste poultry eggshell-derived HAp calcined at 800 °C, 900 °C and 1000 °C was found to be 0.55, 1.26 and 1.65, respectively. An increase in the calcination temperature caused the Ca/P ratio to be much closer to 1.67 which was due to the presence of other phases, such as monetite and calcium hydrogen phosphate hydrate, limiting the achievement of the anticipated stoichiometry ratio.[73] Opposite results were seen in the work by Sanosh *et al.*, where the Ca/P ratio of sol–gel-prepared synthetic nHAp was evaluated with respect to calcination temperature from 65 °C to 800 °C. Based on the results, the Ca/P ratio of nHAp calcined at 65 °C was very near to 1.67 but increased with an increase in the calcination temperature. The formation of minor amounts of CaO at temperatures of 700 °C and above caused this deviation in the Ca/P ratio from the theoretical value, which was also reported in other studies.[74] In our study, the deviation in the Ca/P ratio may be due to several factors given that the amount of eggshell was taken based on the assumption of 97% Ca present in the eggshell. Besides, at 900 °C, nHAp became more crystalline and uniformly structured, which resulted in a Ca/P ratio closer to 1.67.

3.5 DLS hydrodynamic size and surface charge

The hydrodynamic size and surface charge (zeta potential) of the synthesized nHAp samples were measured using a DLS particle size analyzer, as shown in Fig. 7. Before the analysis, the samples were sonicated with DI water at their natural pH to prevent particle agglomeration. The obtained hydrodynamic size of the samples followed the order of nHAp900 (792 nm) > nHAp600 (571 nm) > nHAp300 (276 nm) > nHAp100 (216 nm), which is consistent with the findings through FESEM image-based particle size measurements.

Zeta potential plays a crucial role in determining particle stability in solution, which is influenced by factors such as soluble electrical conductivity, ion concentration, and solvent pH. The zeta potential value is closely related to both the suspension stability and the surface characteristics of particles, making it a significant contributor to overall particle stability in solution. Finding the surface charge of the nanoparticles to be employed as a drug carrier is essential for drug delivery applications.[75,76] Thus, the surface functionality and stability of the synthesized nHAp samples were evaluated in terms of zeta potential. The obtained results suggest that the nHAp100 particles possess excellent stability (−69.92 mV), the nHAp900 particles exhibit good stability (−45.02 mV), the nHAp600 particles demonstrate moderate stability (−31.10 mV), and the nHAp300 particles show incipient stability (−9.98 mV).[77]

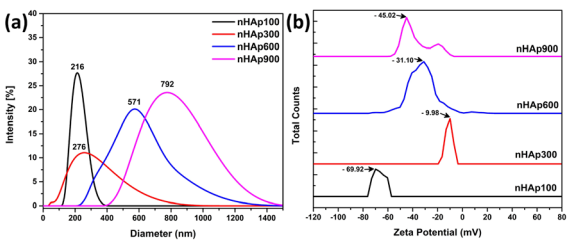

Fig. 7 (a) DLS hydrodynamic size and (b) surface charge analysis of nHAp samples.

3.6 *In vitro* studies

3.6.1 Bio-activity study. In the case of bio-materials such as HAp, the formation of apatite in contact with body fluid is an exigent criterion when used as a bone-repairing material.[78] The appearance of apatite elucidates the bone-bonding ability of bio-materials.[2]

Herein, the bio-activity of the prepared HAp samples was evaluated by FESEM imaging analysis based on their immersion in SBF solution for 21 days. Taking a closer look at the FESEM images, as shown in Fig. 8, the formation of an apatite layer on the powdered nHAp samples was evident. The discrete particles of all the samples were found to be covered after 21 days of immersion in SBF solution, which is due to the attachment of apatite to the nHAp particles. The deposition of an apatite layer on the nHAp particles is due to the interaction of the positive Ca and negative P sites in nHAp with the negative PO_4^{3-} and positive Ca^{2+} charged sites in SBF. The combination of the opposite charged sites induced the nucleation of apatite, and the continuation of this resulted in the super-saturation of the discrete nHAp particles by the apatite layer.[2,78–80]

3.6.2 Cytocompatibility assessment. The cytocompatibility assessment of the synthesized HAp samples is presented in Fig. 9. The optical images represent the interaction of the Vero cell line with the HAp samples (Fig. 9a–d) and control, which was solvent negative and positive (Fig. 9e and f). The assessment was based on the percentage of living cells, also known as cell viability, as shown in Table 3.

According to the results, all the nHAp samples showed no signs of cytotoxicity, and their cell viability was more than 95%.

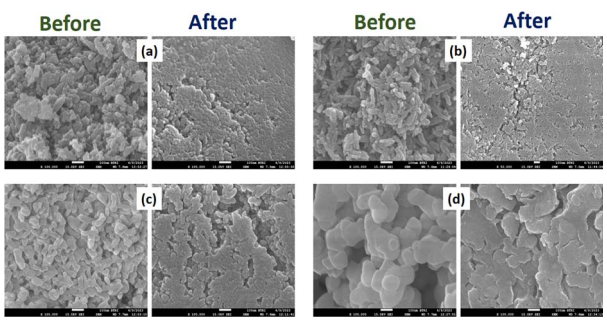

Fig. 8 FESEM images of the nHAp samples before and after immersion in SBF for 21 days: (a) nHAp100, (b) nHAp300, (c) nHAp600 and (d) nHAp900.

Open Access Article. Published on 12 December 2023. Downloaded on 2/8/2026 7:38:46 PM.
This article is licensed under a Creative Commons Attribution-NonCommercial 3.0 Unported Licence.

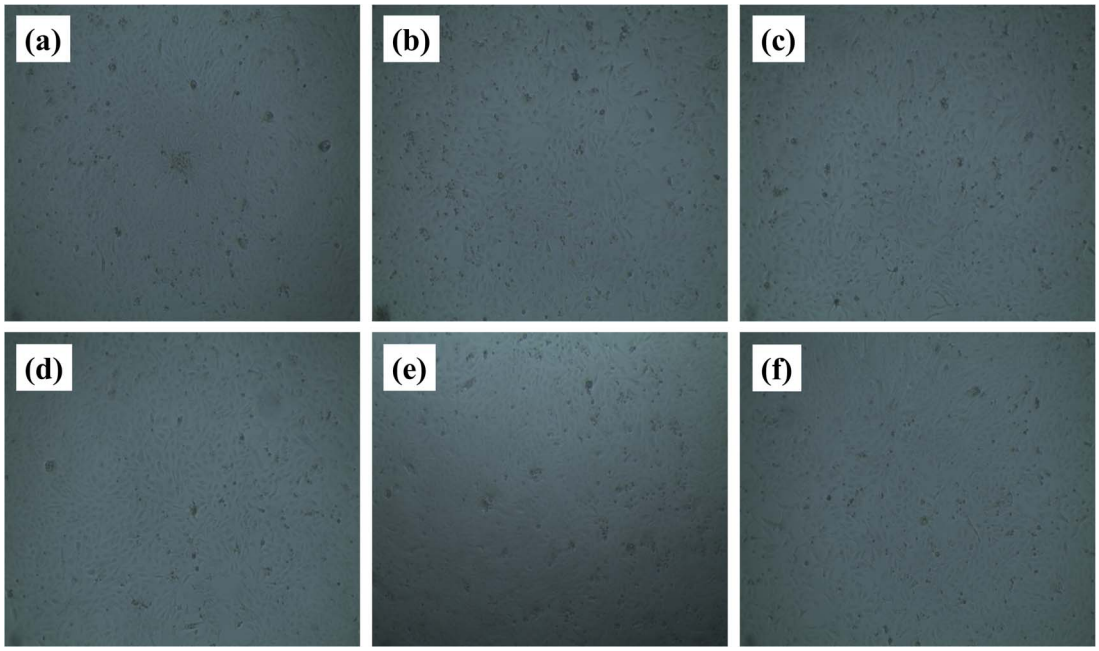

Fig. 9 Optical microscopy images of Vero cells cultured with (a) nHAp100, (b) nHAp300, (c) nHAp600, (d) nHAp900, (e) negative control and (f) positive control. Sample amount 25 μL each and incubation period 48 h.

Table 3 Cytocompatibility assessment of nHAp samples incubated with Vero cell line

Sample ID	Survival of cells	Remarks
Control (−ve) (solvent)	100%	All the samples showed no signs of cytotoxicity
Control (+ve) (solvent)	100%	
nHAp100	>95%	
nHAp300	>95%	
nHAp600	>95%	
nHAp900	>95%	

Based on ISO 10993-5: 2009, a material is termed cytotoxic if it has cell viability of less than 70%.[81] Thus, according to this definition, the synthesized nHAp samples are very cytocompatible with a cell viability not less than 95%.

3.6.3 Anti-bacterial activity. As a gold standard biomaterial, the antibacterial property of HAp adds further value to its application. The antibacterial property of HAp is evident from the literature.[21,82,83] Given that our synthesized nHAp samples were found to be nano-structured based on the particle size measurements using the FESEM images, we explored their antibacterial activity, which will be an exciting addition of properties to the bio-material. Fig. 10 shows the results of the antibacterial activity of nHAp100, nHAp300, nHAp600, nHAp900, Kanamycin (positive control) and DMSO (negative control).

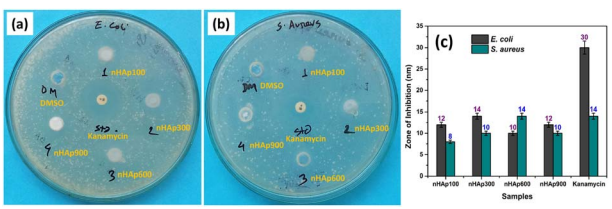

Fig. 10 Anti-bacterial activity of the prepared nHAp samples against: (a) *E. coli* and (b) *S. aureus* and (c) comparison based on zone of inhibition.

Compared to the standard kanamycin (30 μg), the nHAp samples (400 μg mL^{-1}) exhibited significant antibacterial efficacy against both Gram −ve (*E. coli*) and Gram +ve bacteria (*S. aureus*). The highest activity against *E. coli* and *S. aureus* was shown by HAp300 (14 nm) and HAp600 (14 nm), respectively. The antibacterial activity of kanamycin and HAp600 was the same for Gram-positive bacteria. A deeper look into the results revealed that the Gram-negative bacteria were slightly more susceptible to the HAp samples. Similar phenomena were also reported by Ragab *et al.*[84]

3.6.4 Hemolytic study. After being implanted in the body, the nHAp carriers interact with plasma proteins and red blood cells (RBCs). Thus, it was important to study how blood interacts with the nHAp carriers in a specific environment. Fig. 11 represents the hemolytic study of the four HAp samples, each with a concentration of 400 μg mL^{-1} in PBS. As evident in this study, the nHAp carriers did not cause hemolysis in human RBCs. According to the ASTM standard, a hemolysis percentage of less than 5% is considered highly hemocompatible.[85,86] The absence of hemolysis associated with nHAp is attributed to its structural similarity to natural bone and the presence of charged surface sites, which prevent interactions with red blood cells (RBCs).[15]

3.6.5 *In vitro* drug release study. With the aim of investigating the drug release profile of the prepared nHAp samples,

© 2023 The Author(s). Published by the Royal Society of Chemistry

Open Access Article. Published on 12 December 2023. Downloaded on 2/8/2026 7:38:46 PM.
This article is licensed under a Creative Commons Attribution-NonCommercial 3.0 Unported Licence.

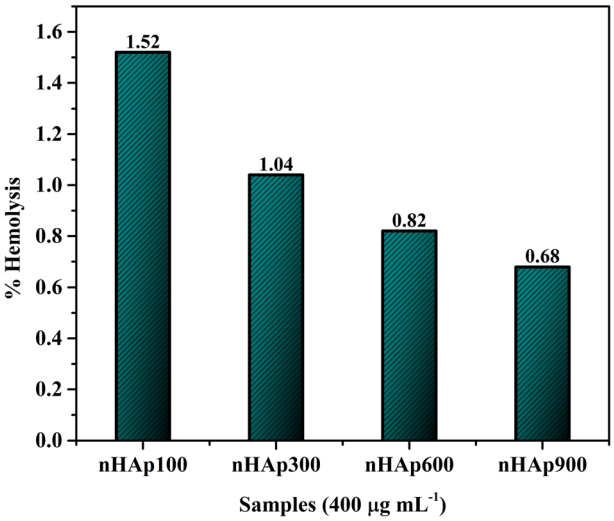

Fig. 11 Hemolysis study of the synthesized nHAp carriers having concentrations of 400 μg mL^{-1} each.

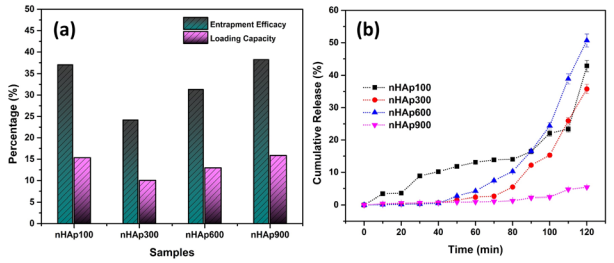

Fig. 12 (a) DOXh loading study of the nHAp samples in terms of entrapment efficacy and loading capacity and (b) *in vitro* cumulative release% of DOXh from nHAp samples (pH = 7.4 at 37 °C).

firstly their drug loading efficacy was examined given that it impacts the release profile to a great extent.[87] The loading characteristics were evaluated in terms of entrapment efficacy (EE) and loading capacity (LC), as shown in Fig. 12a.

The highest EE (38.24%) was found for nHAp900, which was slightly higher than that of nHAp100 (37.01%), followed by nHAp600 and nHAp300. A similar pattern was observed for the LC of the samples. With an increase in the calcination temperature from 300 °C to 900 °C, a gradual increase in EE and LC was obtained except for nHAp100.

Fig. 12b presents the *in vitro* DOXh release in SBF at 37 °C with respect to time. The release was measured at intervals of 10 min up to 120 min under constant stirring. A similar release pattern was observed for nHAp300, nHAp600 and nHAp900, where almost the same amount of release was observed up to 40 min. In contrast, nHAp100 showed a higher initial release than the other samples until nHAp600 surpassed it after 70 min. Overall, a higher release was found for nHAp600, followed by nHAp100 and nHAp300. Although HAp900 showed the highest EE and LC, its cumulative release percentage was the lowest among the nHAp samples. Within 120 min, nHAp900 showed only 5.40% release, whereas nHAp600 showed 50.68% release. Interestingly, no initial burst release of DOXh was observed for any of the nHAp samples, although nHAp100 showed a slightly higher release, which does not depict burst release. This may be due to the fact that our loading protocol involved continuous stirring of the powdered nHAp sample and the drug solution, followed by multiple washings of the drug-loaded nHAp with DI and acetone, which eliminated the possibility of any slack binding of the drug molecules. Based on the observations, increased calcination temperatures lowered the release except for nHAp600. Thus, to achieve sustained release, nHAp900 will be the most suitable, having the highest loading and lowest release percentage.

3.6.6 Drug release kinetic study. Drug release kinetics is an important phenomenon that needs to be considered for an effective understanding of the pattern of release of a drug. This knowledge also helps in understanding the interaction between carriers and drugs, which ultimately results in the design of an effective formulation.[88] According to Dash *et al.*, there are three categories of approaches for investigating the drug release kinetics, including statistical, model-independent, and model-independent.[89] Herein, we adopted model-dependent approaches for investigating the DOXh release kinetics of the synthesized nHAp samples.

3.6.6.1 Zero-order kinetic model. The zero-order kinetic model represents the drug delivery system, where the release of drugs is constant and does not depend on concentration. This relation is exploited to describe the drug release of several pharmaceutical systems, such as transdermal, matrix tablet, and osmotic systems.[89] The simplest form of this model is represented as follows:

$$C_t = C_o + K_o t \quad (12)$$

where C_t refers to the amount of drug released or dissolved at time t, C_o is the initial amount of drug present in the solution (which is zero most of the time) and K_o is the zero-order rate

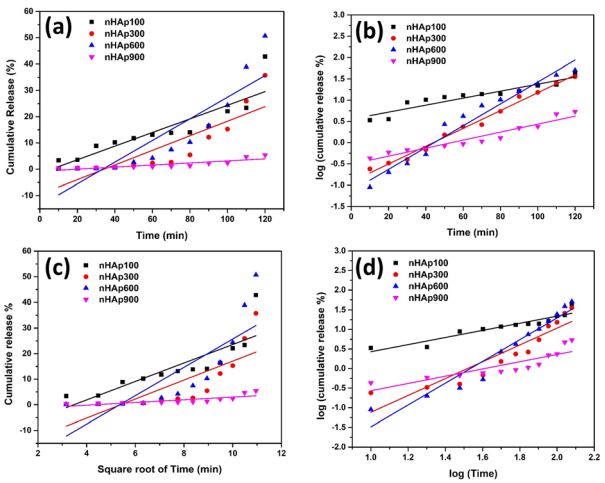

Fig. 13 *In vitro* DOXh release kinetics from nHAp samples: (a) zero-order model, (b) first-order model, (c) Higuchi model and (d) Korsmeyer–Peppas model.

Open Access Article. Published on 12 December 2023. Downloaded on 2/8/2026 7:38:46 PM.
This article is licensed under a Creative Commons Attribution-NonCommercial 3.0 Unported Licence.

Table 4 Kinetic model parameters for DOXh release from nHAp samples

	Zero-order model		First-order model		Higuchi model		Korsmeyer-Peppas model		
Sample	K_o	R^2	K_1	R^2	K_H	R^2	K_{KP}	n	R^2
HAp100	0.2599	0.7578	0.01895369	0.8774	3.6156	0.6789	0.6529	0.9087	0.8878
HAp300	0.2782	0.7112	0.04833997	0.9889	3.7084	0.5761	0.0381	2.1524	0.8491
HAp600	0.4125	0.7628	0.0591871	0.9627	5.5417	0.6305	0.0140	2.7813	0.9316
HAp900	0.0393	0.7078	0.02171729	0.9253	0.5272	0.5826	0.2244	0.9282	0.7228

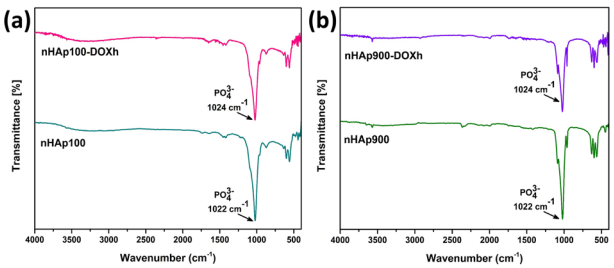

Fig. 14 FTIR spectra before and after DOXh loading on (a) nHAp100 and (b) nHAp900.

constant.[90] The cumulative DOXh release from the nHAp samples was plotted against time, as shown in Fig. 13a. The gradient of the graph represents the zero-order rate constant (K_o), while the correlation coefficient determines the appropriateness of this kinetic model. The values of K_o and R^2 are shown in Table 4.

3.6.6.2 First-order kinetic model. Drug delivery systems in which the adsorption and/or elimination of drugs are associated and the rate of release is dependent on the concentration are better explained by this model. The most primitive form of the first-order kinetic equation can be found in the report by Noyes *et al.*[91] and the first application of this kinetics used in drug dissolution was found in the work of Gibaldi *et al.*[92] Typically the release of water-soluble drugs from porous materials is well described by this kinetic model,[89] and its simplified form equation can be expressed as follows:

$$\frac{dC}{dt} = K_1 C \quad (13)$$

This equation can also be expressed as

$$\log C = \log C_o - \frac{K_1 t}{2.303} \quad (14)$$

where K_1 is the first-order rate constant. The fitting of the plot of log cumulative release% against time will result in a slope that is equal to $-K_1/2.303$. The plot is shown in Fig. 13b and the values of R^2 and K_1 are tabulated in Table 4.

3.6.6.3 Higuchi kinetic model. Professor Takeru Higuchi introduced a mathematical equation that characterizes the release of drugs from matrix systems, specifically addressing the release of both water-soluble and poorly soluble drugs from semi-solid and solid matrix systems.[93,94] The simplified Higuchi model, which relies on Fickian diffusion principles, elucidates drug release kinetics by establishing a linear correlation between the cumulative drug release and the square root of time.[2] The equation is as follows:

$$C = K_H \times t^{1/2} \quad (15)$$

where C is the cumulative drug release% and K_H is the Higuchi constant. The fitting of the plot between cumulative drug release% against square root of time resulted in a linear relationship, as shown in Fig. 13c, where the slope represents the Higuchi constant. The values of K_H and R^2 of the HAp samples are tabulated in Table 4.

3.6.6.4 Korsmeyer-Peppas kinetic model. To elucidate both Fickian and non-Fickian drug release from either swelling or non-swelling polymeric systems, Korsmeyer and Peppas introduced a pragmatic formula as depicted below:[95]

$$C = K_{KP} \times t^n \quad (16)$$

where K_{KP} is the Korsmeyer–Peppas constant and n refers to the diffusional exponent, which describes the drug release mechanism. The significance of n is as follows: when $n < 0.5$, it represents quasi Fickian diffusion but $n = 0.5$ refers to Fickian diffusion; when n is greater than 0.5 but less than 1, it refers to non-Fickian diffusion; and when $n = 1$ and $n > 1$, it represents the case II transport and super case II transport, respectively.[88] The fitting of the plot between log cumulative release% and log time produced a linear relationship, as shown in Fig. 13d.

The kinetic parameters obtained from the model equations are represented in Table 4.

The best fitted model was chosen according to the highest correlation coefficient (R^2) value. According to the data obtained, the first-order model is the best-fitted kinetic model that describes the DOXh release from the nHAp samples, except nHAp100, which was best described by the Korsmeyer–Peppas model. The value of n for DOXh release from nHAp100 and nHAp900 was $0.5 < n < 1$, which depicts non- Fickian diffusion (non-swellable matrix diffusion). Alternatively, for nHAp300 and nHAp600, the value of n is greater than 1, which indicates super case II transport (relaxation/erosion drug release mechanism).[88]

3.7 XPS and FTIR analysis for drug loading mechanism

To comprehend the adsorption mechanism of DOXh on nHAp, XPS and FTIR analysis were carried out. nHAp100 and nHAp900, which showed the highest and closest loading percentage, were considered for this analysis. Similarly, after

© 2023 The Author(s). Published by the Royal Society of Chemistry

Open Access Article. Published on 12 December 2023. Downloaded on 2/8/2026 7:38:46 PM.
This article is licensed under a Creative Commons Attribution-NonCommercial 3.0 Unported Licence.

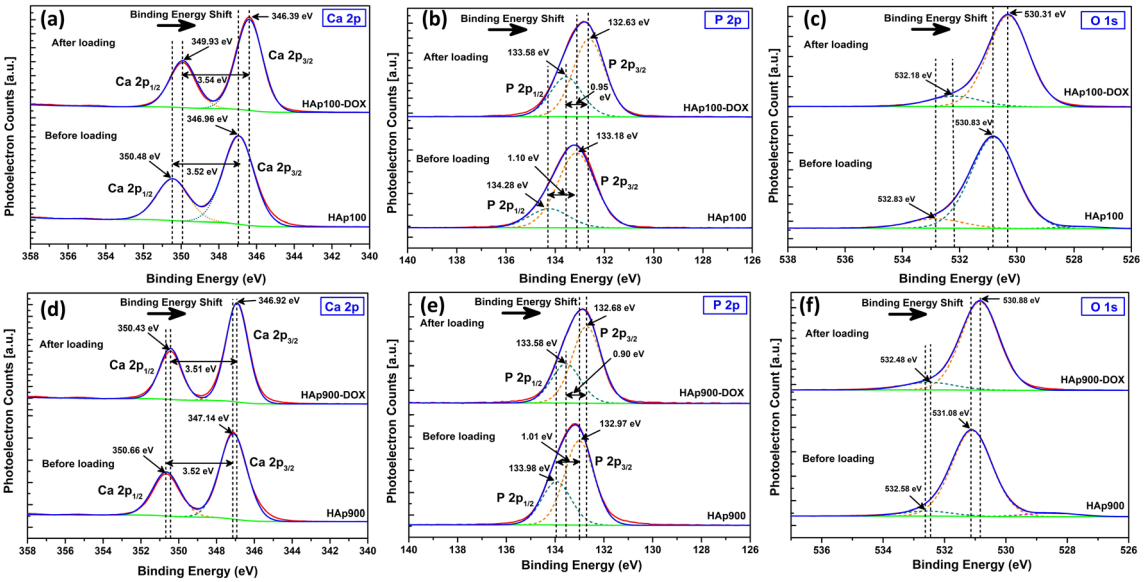

Fig. 15 XPS core level spectra of Ca 2p, P 2p and O 1s before and after DOXh loading on (a–c) nHAp100 and (d–f) nHAp900, respectively.

DOXh loading, the nHAp100-DOXh and nHAp900-DOXh samples were also considered, respectively. Fig. 14 represents the FTIR spectra before and after DOXh loading of nHAp100 and nHAp900. In both cases, the predominant absorption band, which is due to the presence of the PO_4^{3-} group, shifted towards the higher wavenumber region. This suggests the formation of hydrogen bonds between the nHAp and DOXh molecules.

A shift in the binding energy (BE) after DOXh loading was observed during the XPS analysis. Fig. 15 represents the XPS core level spectra of the major elements of nHAp100 and nHAp900 and the corresponding DOXh-loaded samples.

The deconvoluted core level spectra of Ca 2p for nHAp100 shows (Fig. 15a) a doublet separation of 3.52 eV (position of Ca $2p_{1/2}$ and Ca $2p_{3/2}$ at 350.48 eV and 346.96 eV, respectively).[50] In the case of nHAp100-DOXh, a shift in the BE was observed, where Ca $2p_{1/2}$ and Ca $2p_{3/2}$ were observed at 349.93 eV and 346.39 eV with a doublet separation of 3.54 eV, respectively. In the case of nHAp900, Ca $2p_{1/2}$ and Ca $2p_{3/2}$ were observed at 350.66 eV and 347.14 eV (Fig. 15d) with a doublet separation of 3.52 eV, whereas after DOXh loading, the peaks of Ca $2p_{1/2}$ and Ca $2p_{3/2}$ shifted to 350.43 eV and 346.92 eV with a doublet separation of 3.51 eV, respectively. In both cases, the BE shifted to a lower BE.

In the case of the P 2p XPS peak, both nHAp100 and nHAp100-DOXh showed spin–orbit splitting into P $2p_{1/2}$ and P $2p_{3/2}$ with a doublet separation of 1.10 eV and 0.95 eV, respectively (Fig. 15b). In the case of nHAp900 and nHAp900-DOXh, this doublet separation was 1.01 eV and 0.90 eV, respectively (Fig. 15e). Both nHAp100 and nHAp900 showed a shift in BE after DOXh loading. In the O 1s core level spectra of nHAp100 and nHAp900 and the corresponding DOXh-loaded samples (Fig. 15c and f, respectively), a shift in the BE was also evident.

This shift in the BE towards a lower energy for all the peaks after DOXh loading depicts the chemical interaction of the Ca^{2+}, PO_4^{3-} and OH^- sites of nHAp with DOXh, which led to the adsorption of DOXh on nHAp.[96]

4. Conclusion

The present study investigated how DOXh is loaded in and released from nHAp that underwent calcination at four different temperatures. The synthesis of nHAp involved the utilization of WCE through the wet chemical precipitation method. With an increase in calcination temperature, a variation in the crystallographic parameters and loading and release was observed. The DOXh loading decreased as the calcination temperature of nHAp increased from 100 °C to 300 °C but increased for nHAp600, reaching its peak value for nHAp900. A shift in the characteristic peaks after DOXh loading was observed by FTIR and XPS analysis, which depicted the chemical interaction of the nHAp carriers and DOXh. In the case of the release of DOXh, elevated calcination temperatures led to a decrease in its release, except in the case of nHAp600. Thus, to achieve sustained release, nHAp900 appears to be the most appropriate candidate due to its combination of the highest loading and lowest release percentage. Furthermore, the WCE-derived nHAp carriers were cytocompatible, hemocompatible, bioactive, and most importantly bactericidal against both Gram-negative (*E. coli*) and Gram-positive (*S. aureus*) bacteria.

Author contributions

M. B. M. conceived the idea, formal analysis, wrote and finalized the manuscript; M. N. I. collected the raw materials and carried out the synthesis; F. C. carried out FESEM, EDX and bioactivity study; M. N. U. carried out hemolysis and antibacterial analysis; M. S. H. carried out XRD; M. M. carried out DLS and zeta potential analysis; U.S.A. carried out XPS analysis; N. H. T.

Open Access Article. Published on 12 December 2023. Downloaded on 2/8/2026 7:38:46 PM. This article is licensed under a Creative Commons Attribution-NonCommercial 3.0 Unported Licence.

carried out Raman analysis; A. F. M. M. R. resources; S. A. supervised the entire work. The results were jointly examined, and the manuscript was a product of teamwork that included all authors. Each author has reviewed and approved the final published version of the manuscript.

Conflicts of interest

There are no conflicts to declare.

Acknowledgements

We acknowledge the support from Bangladesh Council of Scientific and Industrial Research (BCSIR) through R&D project (ref. no. 39.02.0000.011.14.134.2021/900; Date: 30.12.2021). We would like to extend our gratitude to IGCRT, Dhaka Lab, BTRI, CARF and CARS.

Notes and references

1 J.-Q. Liu, M. Li, S. Yin, X. Chen, M. Li, Y. Pan, Y. Peng, J. Sun and A. Kumar, *J. Mater. Chem. B*, 2022, **10**, 5105–5128.
2 G. S. Kumar, R. Govindan and E. K. Girija, *J. Mater. Chem. B*, 2014, **2**, 5052–5060.
3 D. P. Lew and F. A. Waldvogel, *Lancet*, 2004, **364**, 369–379.
4 I. G. Sia and E. F. Berbari, *Best Pract. Res. Clin. Rheumatol.*, 2006, **20**, 1065–1081.
5 N. Kavanagh, E. J. Ryan, A. Widaa, G. Sexton, J. Fennell, S. O'Rourke, K. C. Cahill, C. J. Kearney, F. J. O'Brien and S. W. Kerrigan, *Clin. Microbiol. Rev.*, 2018, **31**, 000844.
6 C. Zhong, Y. Wu, H. Lin and R. Liu, *Composites, Part B*, 2022, 110428.
7 A. L. L. Lima, P. R. Oliveira, V. C. Carvalho, S. Cimerman and E. Savio, *Braz. J. Infect. Dis.*, 2014, **18**, 526–534.
8 S. K. Nandi, P. Mukherjee, S. Roy, B. Kundu, D. K. De and D. Basu, *Mater. Sci. Eng. C*, 2009, **29**, 2478–2485.
9 M. Hasegawa, A. Sudo, V. S. Komlev, S. M. Barinov and A. Uchida, *J. Biomed. Mater. Res. B Appl. Biomater.*, 2004, **70**, 332–339.
10 H. Alvarez, C. Castro, L. Moujir, A. Perera, A. Delgado, I. Soriano, C. Evora and E. Sanchez, *J. Biomed. Mater. Res. B Appl. Biomater.*, 2008, **85**, 93–104.
11 V. Mouriño and A. R. Boccaccini, *J. R. Soc. Interface*, 2010, **7**, 209–227.
12 J. S. Price, A. F. Tencer, D. M. Arm and G. A. Bohach, *J. Biomed. Mater. Res.*, 1996, **30**, 281–286.
13 Z. Ruszczak and W. Friess, *Adv. Drug Deliv. Rev.*, 2003, **55**, 1679–1698.
14 C. R. Arciola, D. Campoccia and L. Montanaro, *Nat. Rev. Microbiol.*, 2018, **16**, 397–409.
15 N. H. Alotaibi, M. U. Munir, N. K. Alruwaili, K. S. Alharbi, A. Ihsan, A. S. Almurshedi, I. U. Khan, S. N. A. Bukhari, M. Rehman and N. Ahmad, *Pharmaceutics*, 2022, **14**, 975.
16 İ. Gürsel, F. Korkusuz, F. Türesin, N. G. Alaeddinoğlu and V. Hasırcı, *Biomaterials*, 2000, **22**, 73–80.
17 L. Fan, J. Zhang and A. Wang, *J. Mater. Chem. B*, 2013, **1**, 6261–6270.
18 S. Sultana, M. S. Hossain, M. Mahmud, M. B. Mobarak, M. H. Kabir, N. Sharmin and S. Ahmed, *RSC Adv.*, 2021, **11**, 3686–3694.
19 S. Lara-Ochoa, W. Ortega-Lara and C. E. Guerrero-Beltrán, *Pharmaceutics*, 2021, **13**, 1642.
20 M. B. Mobarak, M. S. Hossain, Z. Yeasmin, M. Mahmud, M. M. Rahman, S. Sultana, S. M. Masum and S. Ahmed, *J. Mol. Struct.*, 2022, **1252**, 132142.
21 M. S. Hossain, M. A. A. Shaikh, S. A. Jahan, M. Mahmud, M. B. Mobarak, M. S. Rahaman, M. N. Uddin and S. Ahmed, *RSC Adv.*, 2023, **13**, 9654–9664.
22 M. S. Hossain, M. Mahmud, S. Sultana, M. Bin Mobarak, M. S. Islam and S. Ahmed, *R. Soc. Open Sci.*, 2021, **8**, 210684.
23 M. Hossain, M. Mahmud, M. B. Mobarak and S. Ahmed, *Chem. Pap.*, 2021, 1–13.
24 M. Hossain, M. Mahmud, M. B. Mobarak, S. Sultana, M. Shaikh, A. Ali and S. Ahmed, *Chem. Pap.*, 2022, 1–7.
25 M. S. Hossain, M. M. Hasan, M. Mahmud, M. B. Mobarak and S. Ahmed, *Chem. Pap.*, 2023, **77**, 463–471.
26 O. P. Oni, Y. Hu, S. Tang, H. Yan, H. Zeng, H. Wang, L. Ma, C. Yang and J. Ran, *Mater. Chem. Front.*, 2023, **7**, 9–43.
27 G. Devanand Venkatasubbu, S. Ramasamy, V. Ramakrishnan and J. Kumar, *3 Biotech*, 2011, **1**, 173–186.
28 X.-J. Ji, L. Gao, J.-C. Liu, J. Wang, Q. Cheng, J.-P. Li, S.-Q. Li, K.-Q. Zhi, R.-C. Zeng and Z.-L. Wang, *Colloids Surf. B Biointerfaces*, 2019, **179**, 429–436.
29 U. Joosten, A. Joist, G. Gosheger, U. Liljenqvist, B. Brandt and C. von Eiff, *Biomaterials*, 2005, **26**, 5251–5258.
30 S. Tang, B. Tian, Q.-F. Ke, Z.-A. Zhu and Y.-P. Guo, *RSC Adv.*, 2014, **4**, 41500–41509.
31 F. Hilbrig and R. Freitag, *Biotechnol. J.*, 2012, **7**, 90–102.
32 K. Baskar, B. Saravana Karthikeyan, I. Gurucharan, S. Mahalaxmi, G. Rajkumar, V. Dhivya and A. Kishen, *Int. Endod. J.*, 2022, **55**, 89–102.
33 S. A. Rani, K. Rajkumar, B. S. Karthikeyan, S. Mahalaxmi, G. Rajkumar and V. Dhivya, *J. Mech. Behav. Biomed. Mater.*, 2023, **141**, 105748.
34 S. Kumar, G. M. Kumar, K. Shahapurkar, V. Tirth, A. Algahtani, T. Al-Mughanam, A. H. Alghtani and H. A. Murthy, *J. Mech. Behav. Biomed. Mater.*, 2023, 105963.
35 A. L. Angelette, L. L. Rando, R. D. Wadhwa, A. A. Barras, B. M. Delacroix, N. C. Talbot, S. Ahmadzadeh, S. Shekoohi, E. M. Cornett and A. M. Kaye, *Adv. Ther.*, 2023, **40**, 1366–1378.
36 A. R. Zelmer, R. Nelson, K. Richter and G. J. Atkins, *Bone Res.*, 2022, **10**, 53.
37 B. Spellberg and B. A. Lipsky, *Clin. Infect. Dis.*, 2012, **54**, 393–407.
38 L. Ding, P. Zhang, X. Wang and S. Kasugai, *Clin. Implant Dent. Rel. Res.*, 2019, **21**, 154–159.
39 X. Wang, H. Xu, Y. Zhao, S. Wang, H. Abe, M. Naito, Y. Liu and G. Wang, *Mater. Sci. Eng. B*, 2012, **177**, 367–372.
40 R. Ramírez-Agudelo, K. Scheuermann, A. Gala-García, A. P. F. Monteiro, A. D. Pinzón-García, M. E. Cortés and R. D. Sinisterra, *Mater. Sci. Eng. C*, 2018, **83**, 25–34.
41 C. Soriano-Souza, H. Valiense, E. Mavropoulos, V. Martinez-Zelaya, A. M. Costa, A. T. Alves, M. Longuinho,

© 2023 The Author(s). Published by the Royal Society of Chemistry

Open Access Article. Published on 12 December 2023. Downloaded on 2/8/2026 7:38:46 PM. This article is licensed under a Creative Commons Attribution-NonCommercial 3.0 Unported Licence.

R. Resende, C. Mourão, J. Granjeiro, M. H. Rocha-Leao, A. Rossi and M. Calasans-Maia, *J. Biomed. Mater. Res.*, 2020, **108**, 1351–1362.
42 H. Semyari, M. Salehi, F. Taleghani, A. Ehterami, F. Bastami, T. Jalayer, H. Semyari, M. Hamed Nabavi and H. Semyari, *J. Biomater. Appl.*, 2018, **33**, 501–513.
43 V. Andrei, N. I. Fi□, I. Matei, R. Barabás, L. A. Bizo, O. Cadar, B. A. Bo□ca, N.-I. Farkas, L. Marinca□ and D.-M. Muntean, *Materials*, 2022, **15**, 6225.
44 M. Trzaskowska, V. Vivcharenko and A. Przekora, *Int. J. Mol. Sci.*, 2023, **24**, 5083.
45 M. B. Mobarak, M. S. Hossain, Z. Yeasmin, M. Mahmud, M. M. Rahman, S. Sultana, S. M. Masum and S. Ahmed, *J. Mol. Struct.*, 2022, **1252**, 132142.
46 S. D. Lala, E. Barua, P. Deb and A. B. Deoghare, *Mater. Today Commun.*, 2021, **27**, 102443.
47 A. C. Tas, *Biomaterials*, 2000, **21**, 1429–1438.
48 T. Kokubo, H. Kushitani, S. Sakka, T. Kitsugi and T. Yamamuro, *J. Biomed. Mater. Res.*, 1990, **24**, 721–734.
49 P. Li, C. Ohtsuki, T. Kokubo, K. Nakanishi, N. Soga, T. Nakamura and T. Yamamuro, *J. Am. Ceram. Soc.*, 1992, **75**, 2094–2097.
50 M. B. Mobarak, N. S. Pinky, F. Chowdhury, M. S. Hossain, M. Mahmud, M. S. Quddus, S. A. Jahan and S. Ahmed, *J. Saudi Chem. Soc.*, 2023, 101690.
51 C. Perez, *Acta Biol. Med. Exp.*, 1990, **15**, 113–115.
52 V. P. Padmanabhan, S. N. TSN, S. Sagadevan, M. E. Hoque and R. Kulandaivelu, *New J. Chem.*, 2019, **43**, 18484–18494.
53 R. Yang, R. Wang, S. Abbaspoor, M. Rajan, A. T. Jalil, M. M. Saleh and W. Wang, *Arab. J. Chem.*, 2023, **16**, 104799.
54 D. Dasgupta and A. Patel, *Mater. Adv.*, 2022, **3**, 8220–8228.
55 S. M. Londoño-Restrepo, R. Jeronimo-Cruz, B. M. Millán-Malo, E. M. Rivera-Muñoz and M. E. Rodriguez-García, *Sci. Rep.*, 2019, **9**, 1–12.
56 J. H. G. Rocha, A. F. Lemos, S. Kannan, S. Agathopoulos and J. M. F. Ferreira, *J. Mater. Chem.*, 2005, **15**, 5007–5011.
57 J. Zhan, Y.-H. Tseng, J. C. Chan and C.-Y. Mou, *Adv. Funct. Mater.*, 2005, **15**, 2005–2010.
58 I. Mobasherpour, M. S. Heshajin, A. Kazemzadeh and M. Zakeri, *J. Alloys Compd.*, 2007, **430**, 330–333.
59 G. Xu, I. A. Aksay and J. T. Groves, *J. Am. Chem. Soc.*, 2001, **123**, 2196–2203.
60 E. Garskaite, K.-A. Gross, S.-W. Yang, T. C.-K. Yang, J.-C. Yang and A. Kareiva, *CrystEngComm*, 2014, **16**, 3950–3959.
61 W. Wijesinghe, M. Mantilaka, E. V. A. Premalal, H. Herath, S. Mahalingam, M. Edirisinghe, R. Rajapakse and R. M. G. Rajapakse, *Mater. Sci. Eng. C*, 2014, **42**, 83–90.
62 G. Montes-Hernandez and F. Renard, *J. Phys. Chem. C*, 2020, **124**, 15302–15311.
63 U. Anjaneyulu, D. K. Pattanayak and U. Vijayalakshmi, *Mater. Manuf. Processes*, 2016, **31**, 206–216.
64 J. A. Stammeier, B. Purgstaller, D. Hippler, V. Mavromatis and M. Dietzel, *MethodsX*, 2018, **5**, 1241–1250.
65 J. Xue, A. Farris, Y. Wang, W. Yeh, C. Romany, J. K. Guest, W. L. Grayson, A. S. Hall and T. P. Weihs, *Coatings*, 2020, **10**, 715.
66 A. Gupta, A. Prasad, N. Mulchandani, M. Shah, M. Ravi Sankar, S. Kumar and V. Katiyar, *ACS Omega*, 2017, **2**, 4039–4052.
67 V. P. Padmanabhan, R. Kulandaivelu, D. S. Panneer, S. Vivekananthan, S. Sagadevan and J. A. Lett, *Mater. Res. Innov.*, 2020, **24**(3), 171–178.
68 V. Rodríguez-Lugo, T. V. K. Karthik, D. Mendoza-Anaya, E. Rubio-Rosas, L. S. Villaseñor Cerón, M. I. Reyes-Valderrama and E. Salinas-Rodríguez, *R. Soc. Open Sci.*, 2018, **5**, 180962.
69 Y. C. Teh, C. Y. Tan, S. Ramesh, J. Purbolaksono, Y. M. Tan, H. Chandran, W. D. Teng and B. K. Yap, *Ceramics*, 2014, **58**, 320–325.
70 C. Kothapalli, M. Wei, A. Vasiliev and M. T. Shaw, *Acta Mater.*, 2004, **52**, 5655–5663.
71 I. R. Gibson, S. Ke, S. M. Best and W. Bonfield, *J. Mater. Sci.: Mater. Med.*, 2001, **12**, 163–171.
72 M. B. Mobarak, M. S. Hossain, F. Chowdhury and S. Ahmed, *Arab. J. Chem.*, 2022, **15**, 104117.
73 O. G. Agbabiaka, I. O. Oladele, A. D. Akinwekomi, A. A. Adediran, A. O. Balogun, O. G. Olasunkanm and T. M. A. Olayanju, *Sci. African*, 2020, **8**, e00452.
74 K. P. Sanosh, M.-C. Chu, A. Balakrishnan, T. N. Kim and S.-J. Cho, *Bull. Mater. Sci.*, 2009, **32**, 465–470.
75 S. Safi, F. Karimzadeh and S. Labbaf, *Mater. Sci. Eng. C*, 2018, **92**, 712–719.
76 G. Verma, K. C. Barick, N. G. Shetake, B. N. Pandey and P. A. Hassan, *RSC Adv.*, 2016, **6**, 77968–77976.
77 J. M. Alsharef, M. R. Taha and T. A. Khan, *J. Teknol.*, 2017, **79**, 69–81.
78 S.-L. Bee, Y. Bustami, A. Ul-Hamid, K. Lim and Z. A. Abdul Hamid, *J. Mater. Sci.: Mater. Med.*, 2021, **32**, 106.
79 S. L. Aktuğ, S. Durdu, E. Yalçın, K. Çavuşoğlu and M. Usta, *Mater. Sci. Eng. C*, 2017, **71**, 1020–1027.
80 E. A. Ofudje, A. I. Adeogun, M. A. Idowu and S. O. Kareem, *Heliyon*, 2019, **5**, e01716.
81 I. O. for Standardization, 2009.
82 G. S. Kumar, S. Rajendran, S. Karthi, R. Govindan, E. K. Girija, G. Karunakaran and D. Kuznetsov, *MRS Commun.*, 2017, **7**, 183–188.
83 S. Lamkhao, M. Phaya, C. Jansakun, N. Chandet, K. Thongkorn, G. Rujijanagul, P. Bangrak and C. Randorn, *Sci. Rep.*, 2019, **9**, 4015.
84 H. S. Ragab, F. A. Ibrahim, F. Abdallah, A. A. Al-Ghamdi, F. El-Tantawy, N. Radwan and F. Yakuphanoglu, *IOSR J. Pharm. Biol. Sci.*, 2014, **9**, 77–85.
85 V. Sarath Chandra, G. Baskar, R. V. Suganthi, K. Elayaraja, M. I. Ahymah Joshy, W. Sofi Beaula, R. Mythili, G. Venkatraman and S. Narayana Kalkura, *ACS Appl. Mater. Interfaces*, 2012, **4**, 1200–1210.
86 S. R. Chowdhury, A. Mishra, B. Pradhan and D. Saha, *Wear*, 2004, **256**, 1026–1036.
87 A. Sasireka, R. Rajendran, P. Priya and V. Raj, *ChemistrySelect*, 2019, **4**, 1166–1175.
88 M. P. Paarakh, P. A. Jose, C. M. Setty and G. V. Peterchristoper, *Int. J. Pharm. Res. Technol.*, 2018, **8**, 12–20.

Open Access Article. Published on 12 December 2023. Downloaded on 2/8/2026 7:38:46 PM.
This article is licensed under a Creative Commons Attribution-NonCommercial 3.0 Unported Licence.

89 S. Dash, P. N. Murthy, L. Nath and P. Chowdhury, *Acta Pol. Pharm.*, 2010, **67**, 217–223.
90 K. Huanbutta and T. Sangnim, *J. Drug Delivery Sci. Technol.*, 2019, **52**, 831–837.
91 A. A. Noyes and W. R. Whitney, *J. Am. Chem. Soc.*, 1897, **19**, 930–934.
92 M. Gibaldi and S. Feldman, *J. Pharmaceut. Sci.*, 1967, **56**, 1238–1242.
93 T. Higuchi, *J. Pharmaceut. Sci.*, 1963, **52**, 1145–1149.
94 T. Higuchi, *J. Pharmaceut. Sci.*, 1961, **50**, 874–875.
95 R. W. Korsmeyer, R. Gurny, E. Doelker, P. Buri and N. A. Peppas, *Int. J. Pharm.*, 1983, **15**, 25–35.
96 H. Bensalah, S. A. Younssi, M. Ouammou, A. Gurlo and M. F. Bekheet, *J. Environ. Chem. Eng.*, 2020, **8**, 103807.

© 2023 The Author(s). Published by the Royal Society of Chemistry